

# Semi-supervised Semantic Segmentation of Organs at Risk on 3D Pelvic CT Images

Zhuangzhuang Zhang, Tianyu Zhao, Hiram Gay, Baozhou Sun\*, and Weixiong Zhang\*

**Abstract**—Automated segmentation of organs-at-risk in pelvic computed tomography (CT) images can assist the radiotherapy treatment planning by saving time and effort of manual contouring and reducing intra-observer and inter-observer variation. However, training high-performance deep-learning segmentation models usually requires broad labeled data, which are labor-intensive to collect. Lack of annotated data presents a significant challenge for many medical imaging-related deep learning solutions. This paper proposes a novel end-to-end convolutional neural network-based semi-supervised adversarial method that can segment multiple organs-at-risk, including prostate, bladder, rectum, left femur, and right femur. New design schemes are introduced to enhance the baseline residual U-net architecture to improve performance. Importantly, new unlabeled CT images are synthesized by a generative adversarial network (GAN) that is trained on given images to overcome the inherent problem of insufficient annotated data in practice. A semi-supervised adversarial strategy is then introduced to utilize labeled and unlabeled 3D CT images. The new method is evaluated on a dataset of 100 training cases and 20 testing cases. Experimental results, including four metrics (dice similarity coefficient, average Hausdorff distance, average surface Hausdorff distance, and relative volume difference), show that the new method outperforms several state-of-the-art segmentation approaches.

**Index Terms**—Deep Learning, Generative Adversarial Network, Semi-supervised Learning, Organs-at-risk Segmentation.

## I. INTRODUCTION

ACCURATE delineation of organs-at-risk (OAR) is crucial for maximizing target coverage while minimizing toxicities during radiotherapy treatment planning [4]. As a major treatment for prostate cancer, external beam radiotherapy requires accurate segmentation of the prostate and its nearby organs [6]. Experienced oncologists manually contour these OARs, a common clinical practice that entails three serious drawbacks: 1) it is labor-intensive and time-consuming for physicians to contour multiple organs slice-by-slice; 2) the diverse expertise and experience level of physicians lead to considerable intra-observer variation [5]; 3) low-contrast and

fuzzy boundaries of OARs on medical images cause significant interobserver variation of delineation [1]. Time-consuming manual segmentation processes are inadequate to support adaptive treatment, and both intra- and inter-observer variations result in uncertainty in treatment planning that potentially compromises treatment outcomes. Automated segmentation approaches that can rapidly contour OARs with reliable and robust quality can overcome these drawbacks and make radiotherapy treatment planning accurate and efficient.

Accurate contours of the prostate and other OARs on pelvic computed tomography (CT) images of prostate cancer patients are crucial for their treatment planning [4]. Nevertheless, the automated segmentation of these OARs is challenging because these organs often have low-contrast and fuzzy boundaries with the backgrounds. Moreover, substantial variations in organ size, shape, and intensity also render it technically more challenging for automated segmentation.

Deep learning [8] has been developing rapidly as an enabling technique for various real-world problems in the past decade. It has been extended and applied to medical image semantic segmentation to provide accurate, reliable, and efficient delineation of pelvic CT images [3-6, 9-14]. However, supervised deep learning models usually require massive annotated data to train, a severe bottleneck in the medical imaging area. Unlike daily images, medical images need to be annotated by professionals with specific expertise one slice at a time, making data collection laborious, expensive, and time-consuming. Thus, a lack-of-data bottleneck exists in deep learning-based applications in medical imaging field [6]. In this work, we propose a novel semi-supervised adversarial deep learning approach to the rescue. The new approach is proposed in the context of multi-OARs segmentation on 3D CT images, yet it adequately addresses the serious lack-of-data bottleneck by utilizing un-annotated/synthesized images for training. The bottleneck was broken by two eminent features of the new approach. The first feature is that we leverage adversarial learning scheme to utilize un-annotated data for training. With the first feature, we require less annotations for training, but we still need to collect un-annotated data. When even un-annotated data are not available, the second feature of the new approach saves the day by synthesizing new data to enable the semi-

The paper is submitted for review on xx/xx/2020. This work was supported in part by the Varian Medical Systems through a research grant.

Zhuangzhuang Zhang (email: zhang.zhuangzhuang@wustl.edu) is with Department of Computer Science and Engineering, Washington University, One Brookings Drive, Campus Box 1045, St. Louis, Missouri 63130 USA.

Weixiong Zhang (email: weixiong.zhang@wustl.edu) is with Department of Computer Science and Engineering and Department of Genetics, Washington University, One Brookings Drive, Campus Box 1045, St. Louis, Missouri 63130 USA.

Tianyu Zhao, Hiram Gay, and Baozhou Sun (email: baozhou.sun@wustl.edu) are with Department of Radiation Oncology, Washington University School of Medicine, 4921 Parkview Place, Campus Box 8224, St. Louis, Missouri 63110.

\*: Correspondence to weixiong.zhang@wustl.edu or Baozhou.sun@wustl.edu.

supervised adversarial learning scheme.

The new approach involves of three major parts: a CNN-based segmentation network (*S-net*), a discriminator network (*D-net*) for adversarial learning, and a progressive growth generative adversarial network (PGGAN). *S-net* adopts the residual U-net architecture [15] as its backbone and implements multiple design modifications to produce contours of multi-OARs. *D-net* is introduced for adversarial learning. We formulate the adversarial learning scheme of generative adversarial network (GAN) [16] into the context of semantic segmentation by training *D-net* to distinguish predicted label maps from ground-truth label maps. The PGGAN is introduced to synthesize new un-annotated data that can enable semi-supervised learning when there are no un-annotated data available. With these three parts, our approach tackles the lack-of-data problem by utilizing un-annotated data for semi-supervised adversarial learning and PGGAN-aided data augmentation [17].

We evaluated and compared the new model with several state-of-the-art segmentation methods using four widely used metrics: dice similarity coefficient (DSC), average Hausdorff distance (AHD), average surface Hausdorff distance (ASHD), and relative volume difference (VD).

## II. RELATED WORK

### A. Male Pelvic CT Image Segmentation

The automated segmentation of male pelvic CT images has been a research focus for radiation therapy. Two types of methods have been proposed, multi-atlas-based and learning-based methods. The multi-atlas-based methods typically follow two steps to generate organ segmentation: atlases registration and label fusion [6]. Acosta *et al.* explained different segmentation and evaluation strategies for different organs which fall into this category [1]. While the results of these methods are acceptable, the required manual guidance and registration are costly, which the automated segmentation approaches attempt to address [6, 18].

Machine learning methods, such as Random Forests[11], have been exploited to perform OAR segmentation on medical images [19, 20]. As deep learning methods developed fast in the past decades, they have achieved state-of-the-art performance on many difficult problems [8]. Deep learning models have been applied to medical image segmentation with outstanding performance due to their ability for feature extraction and representation [3, 5, 10, 12, 14, 21, 22]. A fully convolutional network (FCN) [23] was first proposed for daily-life image segmentation, which inspired many medical image segmentation methods. For example, Wang *et al.* [12] proposed a dilated FCN method to perform OAR segmentation on pelvic CT images and achieved a DSC score of 0.85 on the prostate. After Ronneberger *et al.* [15] proposed U-net for medical image segmentation, a few U-net variations performed well for image segmentation [4, 5, 10, 24]. Kazemifar *et al.* developed a 2D U-net-based method for the region of interest (ROI) segmentation on pelvic CT images [5]. Their new approach used a 2D U-net for ROI localization and a 3D U-net for segmentation [4].

Despite that their method has excellent performance on multiple organs, the method trains multiple segmentation networks, one for each organ, which is costly for implementation [4].

It is important to highlight that deep learning methods need a massive amount of training data for building effective models. Obtaining massive datasets is challenging in medical imaging since data annotation requires professional expertise so that data collection is labor-intensive and time-consuming.

### B. Generative Adversarial Network (GAN)

The generative adversarial network (GAN), proposed in 2014 by Goodfellow *et al.* [16], has been extensively studied and applied to many real-world problems. A favorable feature of GAN is its ability to generate data with a desirable distribution [25]. GAN consists of two major components, a generator and a discriminator. The generator is trained to learn a model of given training examples. The discriminator is tasked to learn to distinguish the data produced by the generator from given examples [16]. The two components are trained in an adversarial scheme by which they compete against each other until reaching equilibrium – the generator attempts to produce synthetic data that are as similar to the given examples as possible to fool the discriminator, whereas the discriminator tries to distinguish synthetic data from the genuine ones. Tailored to specific applications, several GAN variations have been proposed, such as conditional GAN (CGAN) [26], progressive growth GAN (PGGAN) [27], and triple GAN[28]. These generative methods perform well for data generation and support unsupervised data augmentation.

Besides generating new data, the idea of adversarial learning also lends itself to supervised learning. Luc *et al.* cast a network for segmentation as the generator and adopt the adversarial learning scheme for semantic segmentation, which performed well on the Pascal VOC 2012 dataset [29]. Hung *et al.* proposed a semi-supervised adversarial segmentation method using images with incomplete annotations for training [30].

## III. THE METHOD

### A. Overview

The system of our new method (Fig. 1) included three major components: segmentation network (*S-net*), discriminator network (*D-net*), and progressive growth GAN (PGGAN) [27]. Our method worked in two modes: 1) PGGAN-aided data augmentation; 2) semi-supervised adversarial learning scheme of *S-net* and *D-net*. We combined the force of two modes to address the lack-of-data bottleneck as follows. Firstly, we trained a CT synthesis PGGAN and synthesized un-annotated CT images, which we later used for the semi-supervised learning part of the framework. Secondly, we designed a semi-supervised adversarial learning scheme involving *S-net* and *D-net*, supported by data from an annotated dataset and PGGAN synthesis. The semi-supervised adversarial learning scheme of the framework enabled utilizing un-annotated data for training, and PGGAN-aided data augmentation mode guaranteed sufficient un-annotated data.

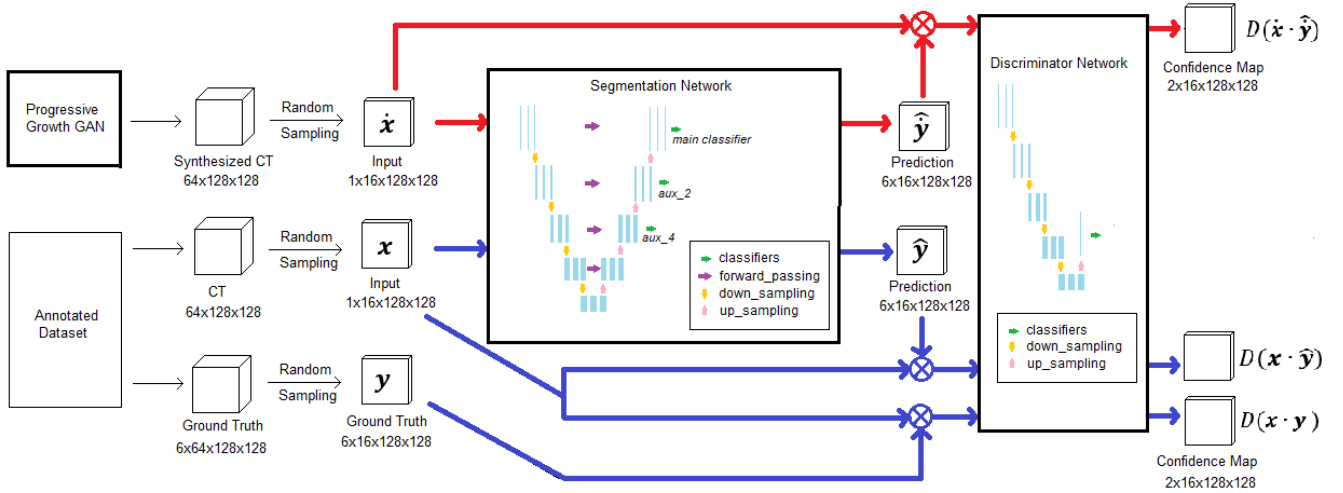


Fig. 1. Workflow of the proposed semi-supervised learning method

The framework was designed for three scenarios: (1) when data annotations are unavailable, yet un-annotated data are available, the framework can utilize un-annotated data for training with the semi-supervised adversarial learning scheme; (2) when there is a lack-of-data problem in general, which means un-annotated data are also unavailable, the framework can synthesize un-annotated data with the help of PGGAN; (3) when available data are sufficient for learning, the framework can use synthesized un-annotated data to activate semi-supervised learning and further boost the learning outcome.

### B. Residual U-net Backbone with Auxiliary Classifiers

The segmentation network of the approach adopted the residual U-net [2] architecture as its backbone. The residual connection allowed the feature maps to bypass the non-linear transformations with an identity mapping. This design was more than regular skip connections in the way that it reformulated the layers as learning residual functions [31]. The residual U-net in *S-net* took  $16 \times 128 \times 128$  CT volumes (16 slices of 128 by 128 CT scans) with one channel as its input. It output  $16 \times 128 \times 128$  segmentation volumes with six channels, one for each of the OARs and the background. With the generic U-net [15] architecture, the segmentation network first down-sampled the input for feature extraction, then up-sampled the extracted feature maps to scale back to the original size and perform classification. During the up-sampling process, feature maps from the down-sampling path were passed forward for concatenation as guidance for high-resolution spatial context information [23]. Along the down-sampling path of the original U-net [15], multiple stride-2 max-pooling layers were used to shrink feature maps, which caused spatial information loss [32]. To preserve spatial information, we replaced all the stride-2 max-pooling layers with multi-scale pooling layers developed by the adversarial multi-residual multi-scale pooling MRF-enhanced network (ARPM-net) [7].

In addition to the classifier at the top level (in green in Fig. 1) that performed classification on feature maps in the original resolution ( $16 \times 128 \times 128$ ), *S-net* also implemented two

auxiliary classifiers. The auxiliary classifier  $aux_2$  (in green in Fig. 1) worked on  $8 \times 64 \times 64$  feature maps with 128 channels, and the  $aux_4$  (in green in Fig. 1) processed  $4 \times 32 \times 32$  feature maps with 256 channels. The segmentation outputs of these two auxiliary classifiers were up-sampled by interpolation to rescale to the input dimension of  $16 \times 128 \times 128$ . This architecture design incorporated the compressed feature maps in the final prediction, allowing us to inject supervision into latent spaces [33]. In the original residual U-net [2], there was only one classifier at the last layer of the network, and its outputs determined the loss from ground-truths. When the loss was back-propagated into the network, the supervision was only provided at the last layer. However, with two auxiliary classifiers contributing to the final prediction, supervision was provided not only at the last layer but also at the middle layers. Thus, we injected supervision into latent spaces with our two auxiliary classifiers. The segmentation predictions of  $aux_4$  and  $aux_2$  were weighted by 0.25 and 0.5 in the final label prediction. The final label map predictions were in  $16 \times 128 \times 128$  volumes, with six channels representing the probability of each voxel belonging to each of the six classes.

### C. Progressive Growth GAN-aided CT Synthesis

The generative adversarial network is known for generating synthetic samples from high-dimensional data distributions [25]. The general framework supports the generation of different types of data, and different GAN variations work specifically well on certain data types. Progressive growing generative adversarial network (PGGAN), as a special GAN, is tailored to image syntheses [27]. The PGGAN incrementally generates images with increasingly higher resolution. It first discovers large structures of the image distribution and then shifts attention to increasingly finer details [27].

We adopted the training scheme of the PGGAN and designed the network architecture for synthesizing 3D CT volumes. The generator  $\mathcal{G}$  and the discriminator  $\mathcal{D}$  had mirrored architectures. The training started by generating  $4 \times 4 \times 4$  volumes.  $\mathcal{G}$  took a



$2 \times 2 \times 2$  random noise  $\mathbf{z}$  as its input and output a  $4 \times 4 \times 4$  synthesized volume  $\mathbf{x}'$ .  $\mathcal{D}$  took  $\mathbf{x}'$  or down-sampled real CT volume  $\mathbf{x}$  as its input, and output a prediction of either the input was real ( $\mathbf{x}$ ) or fake ( $\mathbf{x}'$ ). After  $\mathcal{G}$  was well-trained on low-resolution ( $n \times n \times n$ ) volumes, one more up-sampling block was added to  $\mathcal{G}$  and  $\mathcal{D}$  to generate  $2n \times 2n \times 2n$  volumes. This process repeated until the last up-sampling block was added to generate  $64 \times 128 \times 128$  from  $64 \times 64 \times 64$  feature maps. Note that  $64 \times 128 \times 128$  synthesized CT volumes had the same dimensions as real CT volumes, and they were both cropped to  $16 \times 128 \times 128$  before fed into  $S$ -net. Notice that adding randomly initiated layers to well-trained  $\mathcal{G}$  and  $\mathcal{D}$  could be disruptive to reach a training equilibrium. To address this issue, we used the smooth fade-in trick proposed in [27]. We used a linearly increasing weight  $\alpha$  to combine the outputs from an already trained low-resolution layer and a newly added higher-resolution layer [27]. We used the well-trained PGGAN to synthesize 30 CT volumes to aid semi-supervised learning in the subsequent adversarial semantic segmentation training.

#### D. Semi-supervised Adversarial Training

Adversarial training is mainly used for GAN-based data generation [16]. Moreover, it can potentially improve the performance of the original task by using additional, albeit synthesized, data generated from random noises and training examples [7, 21, 29, 34]. Semantic segmentation can be cast as a generative task. Rather than generating new images,  $S$ -net in our application produced segmentation masks that closely resemble manual delineation masks on input CT images.

We added an adversarial learning scheme to the new approach while exploiting two significant merits of adversarial models. Firstly, without  $D$ -net,  $S$ -net was optimized based only on a cross-entropy loss, an element-wise (i.e., pixel or voxel-wise) loss metric widely used for semantic segmentation [23, 35, 36]. Furthermore, we introduced a style-loss calculated by  $D$ -net into the training scheme to help  $S$ -net generating contours that closely resemble manual contours. Secondly, similar to other CNN networks,  $S$ -net was designed for supervised learning, so it cannot make use of un-annotated CT images. However, thanks to the adversarial learning scheme,  $S$ -net can be extended to learn from un-annotated CT images with the help of the discriminator.

The basic adversarial training scheme had four steps:

1. Feed the input CT image  $\mathbf{x}$  forward through  $S$ -net to obtain predicted mask  $\hat{\mathbf{y}} = S(\mathbf{x})$ , where  $S(\cdot)$  represents the forward passing operation of  $S$ -net.
2. Feed the voxel-wise product of  $\mathbf{x} \cdot \hat{\mathbf{y}}$  (fake input) or  $\mathbf{x} \cdot \mathbf{y}$  (real input) into  $D$ -net to obtain a confidence map  $D(\mathbf{x} \cdot \hat{\mathbf{y}})$  or  $D(\mathbf{x} \cdot \mathbf{y})$ , where  $\mathbf{y}$  is the ground truth label map of CT image  $\mathbf{x}$ , and  $D(\cdot)$  represents forward passing operation of  $D$ -net.
3. Compute the loss for  $S$ -net and  $D$ -net. The main objective of the adversarial learning is to train  $S$ -net to generate “fake” segmentation maps that so closely resemble genuine CT images and can fool  $D$ -net and to simultaneously train  $D$ -net to distinguish fake inputs from real CT images.

4. Backpropagate the loss for  $S$ -net and  $D$ -net. The loss for  $S$ -net (denoted as  $\mathcal{L}_S$ ) has two components, i.e., 1) voxel-wise loss (denoted as  $\mathcal{L}_{vox}$ ) between prediction  $\hat{\mathbf{y}}$  and ground-truth  $\mathbf{y}$ , and 2) adversarial loss (denoted as  $\mathcal{L}_{adv}$ ) computed interactively with  $D$ -net. The loss for  $D$ -net (denoted as  $\mathcal{L}_D$ ) is computed based on how well the discriminator can separate fake inputs from real ones. We will show the math in section III.E.

Besides the basic adversarial learning, we also utilized un-annotated CT images as input to  $S$ -net. Un-annotated CT images came from either real CT images without annotation or PGGAN-synthesized CT images. Similarly, we fed the un-annotated CT image  $\hat{\mathbf{x}}$  to  $S$ -net to predict  $\hat{\mathbf{y}} = S(\hat{\mathbf{x}})$ . Since there was no ground-truth  $\mathbf{y}$  for  $\hat{\mathbf{x}}$ , we cannot compute  $\mathcal{L}_{vox}$  with un-annotated CT images, but we can use  $D$ -net to compute  $D(\hat{\mathbf{x}} \cdot S(\hat{\mathbf{x}}))$  and leverage semi-supervised adversarial learning.

#### E. Learning Algorithm

##### 1) Training the Segmentation Network ( $S$ -net)

Inspired by Wei’s work [30],  $S$ -net was trained with three losses: voxel-wise loss  $\mathcal{L}_{vox}$ , adversarial loss  $\mathcal{L}_{adv}$ , and semi-supervised learning loss  $\mathcal{L}_{semi}$ . Start with the voxel-wise loss  $\mathcal{L}_{vox}$ , adopting the adaptively weighted loss function from the ARPM-net [7], the voxel-wise loss function (for each sample) of  $S$ -net is:

$$\ell_{mce}^*(\hat{\mathbf{y}}, \mathbf{y}) = -\sum_{Z \times H \times W} \sum_{c=1}^C w_c \mathbf{y}_c \ln \hat{\mathbf{y}}_c, \quad (1)$$

$$w_c = 2 - DSC_c + \ln \frac{\text{number of voxel of all classes}}{\text{number of voxel of class } c}. \quad (2)$$

In Eq. 1,  $\ell_{mce}^*(\hat{\mathbf{y}}, \mathbf{y})$  is the adaptively weighted multi-class cross-entropy (MCE) loss between the prediction  $\hat{\mathbf{y}}$  and ground-truth  $\mathbf{y}$ ;  $Z$ ,  $H$ , and  $W$  are the depth, height, and width of the 3D CT volume, respective;  $C$  represents the number of classes, and in our case  $C = 6$ ; and  $w_c$  is the adaptive weight of class  $c$ . The adaptive weight is calculated by Eq. 2, where  $DSC_i$  is the current performance (measured by the Dice Similarity Coefficient) for class  $i$ . Combined, we have the voxel-wise loss  $\mathcal{L}_{vox}$  for all  $N$  samples as:

$$\mathcal{L}_{vox} = \sum_{n=1}^N \ell_{MCE}^*(S(\mathbf{x}_n), \mathbf{y}_n). \quad (3)$$

The adversarial learning trained  $S$ -net to generate segmentation predictions that can fool  $D$ -net to classify a synthetic CT image as a real image. The adversarial loss  $\mathcal{L}_{adv}$  measures the difference between the current  $S$ -net and a “perfect generator” that always fools  $D$ -net. Mathematically, the loss can be written as:

$$\ell_{adv} = \ell_{bce}(D(\mathbf{x}_n \cdot S(\mathbf{x}_n)), \mathbf{1}), \quad (4)$$

where  $\mathbf{1}$  represents the target confidence map of  $D$ -net with value 1 (real) for all voxels;  $\ell_{bce}(\cdot)$  is the binary cross-entropy (BCE) loss function:

$$\ell_{bce}(\hat{\mathbf{z}}, \mathbf{z}) = -\sum_{i=1}^{Z \times H \times W} [\mathbf{z}_i \ln \hat{\mathbf{z}}_i + (1 - \mathbf{z}_i) \ln (1 - \hat{\mathbf{z}}_i)], \quad (5)$$

$$\hat{\mathbf{z}} = D(\mathbf{x}_n \cdot S(\mathbf{x}_n)), \quad (6)$$

$$\mathbf{z} = \mathbf{1}. \quad (7)$$

Thus, we have the adversarial loss  $\mathcal{L}_{adv}$  for all  $N$  samples:

$$\mathcal{L}_{adv} = -\sum_{n=1}^N \sum_{Z \times H \times W} \ln(D(\mathbf{x}_n \cdot S(\mathbf{x}_n))). \quad (8)$$

In semi-supervised learning, un-annotated (or synthetic) CT images can be utilized for  $S$ -net training. Since there is no ground-truth available, we cannot compute  $\mathcal{L}_{vox}$  for un-annotated data. However, for an un-annotated image  $\hat{\mathbf{x}}$ , the trained discriminator  $D$ -net generates a confidence map  $D(\hat{\mathbf{x}} \cdot S(\hat{\mathbf{x}}))$ , which can infer the regions that are sufficiently close to ground-truth label maps [30]. These regions are selected based on a preset threshold  $T_{semi}$ . For image  $\hat{\mathbf{x}}$ , we also have the self-taught “ground-truth”  $\tilde{\mathbf{y}}$  as an element-wise set with  $\tilde{\mathbf{y}}^{(z,h,w,c^*)} = 1$  if  $c^* = \operatorname{argmax}_c S(\mathbf{x})^{(z,h,w,c)}$ , where  $z, h, w$ , and  $c$  denote the voxels at the location  $(z, h, w)$  and channel  $c$ , respectively. Thus the semi-supervised loss can be written as:

$$\mathcal{L}_{semi} = -\sum_{n=1}^N \sum_{Z,H,W} \sum_{c=1}^C \mathbf{I}^{(z,h,w)} \cdot \tilde{\mathbf{y}}_n^{(z,h,w,c)} \ln(S(\hat{\mathbf{x}}_n)^{(z,h,w)}), \quad (9)$$

$$\mathbf{I}^{(z,h,w)} = \left( D(\hat{\mathbf{x}}_n \cdot S(\hat{\mathbf{x}}_n))^{(z,h,w)} > T_{semi} \right). \quad (10)$$

The indicator function  $\mathbf{I}^{(z,h,w)}$  in Eq. 10 indicates if  $S$ -net prediction on voxel at  $(z, h, w)$  is sufficiently trustworthy, and threshold  $T_{semi}$  controls the sensitivity [30]. We also pre-set the threshold to be 0.2, as suggested in [30]. The total loss function  $\mathcal{L}_{S-net}$  is a weighted summation of all losses:

$$\mathcal{L}_S = \mathcal{L}_{vox} + \lambda_{adv} \mathcal{L}_{adv} + \lambda_{semi} \mathcal{L}_{semi}. \quad (11)$$

## 2) Training the Discriminator Network ( $D$ -net)

We train  $D$ -net as a competitor against  $S$ -net in adversarial learning [16]. The discriminator learns to separate the label map prediction generated by  $S$ -net from ground-truth. For input CT image  $\mathbf{x}_n$  with its ground-truth label map  $\mathbf{y}_n$ , we use the binary cross-entropy loss function:

$$\mathcal{L}_D = -\sum_{n=1}^N [\ell_{bce}(D(\mathbf{x}_n \cdot \mathbf{y}_n), 1) + \ell_{bce}(D(\mathbf{x}_n \cdot S(\mathbf{x}_n)), 0)]. \quad (12)$$

$D$ -net learns to label all voxels on the confidence map as 1 (real) if the input is the product computed with the ground-truth and 0 (fake) with  $S$ -net prediction. In Wei’s work, they did not encounter the issue that  $D$ -net easily distinguishes whether the probability maps came from the ground truth by detecting the one-hot probability [29, 30], but we encounter this problem. We resolve the issue using the element-wise product of the input CT image and the one-hot encoded label prediction as the input for  $D$ -net.

## IV. EXPERIMENTS

### A. Data Used and Augmentation

The data used in our study consisted of planning CT and structure data from 120 intact prostate cancer patients that were selected retrospectively. All CT images were acquired by a 16-slice CT scanner with an 85 cm bore size (Philips Brilliance Big Bore, Cleveland, OH, US). Contours of the five OARs (prostate, bladder, rectum, left femur, and right femur) were drawn by two radiation oncologists with over ten years’

experience using the Eclipse treatment planning system (Varian Medical Systems, CA).

Each of the 120 patients offered 100-200 slices with a slice thickness of 1.5mm, and every CT slice was translated into a 2D-array with  $512 \times 512$  pixels according to original pixel spacing. We stacked 2D CT slices to build 3D CT volumes concerning the slice thickness. To accommodate the workstation that we use for the experiments, we first center cropped each slice to the size of  $384 \times 384$ , then resized them to  $128 \times 128$  and picked the middle 64 slices from each case. Thus, for every patient, we built the 3D Volume with dimensions of  $64 \times 128 \times 128$ .

We randomly split the data for 120 cases into a train/validation set of 100 cases and a test set of 20 cases. We used the train/validation set with 100 patients to perform 10-fold cross-validation, during which 90 cases were used for training, and 10 cases for validation each time. The test set (with 20 cases) was used for model evaluation and performance comparison. The size of the training set (90 cases) was small and may result in serious over-fitting issues, so we used a random sampling technique for data augmentation. For each training iteration, we randomly picked 16 continuous slices from the  $64 \times 128 \times 128$  CT volumes and cropped the ground-truth label maps accordingly. Thus, each  $64 \times 128 \times 128$  volume can generate 48 different  $16 \times 128 \times 128$  volumes depending on different cropping positions. These smaller volumes may contain different OARs, and the positions of OARs were shifted between volumes cropped from nearby positions. This technique effectively augmented the training data by adding diversity and random translations to fixed organ positions. During the inference and testing phase, each validation/testing case was cropped into four 16-slice volumes and then fed into the model one by one. The outcomes from the network were later stacked together to restore the original dimensions ( $64 \times 128 \times 128$ ) for evaluation.

We set up three configurations of the training set for model comparison: a) 90 annotated cases (*config.A*); b) 60 annotated cases (randomly selected from the 90 cases) plus 30 cases without annotation (*config.B*); and c) 90 annotated cases plus 30 PGGAN-synthesized un-annotated cases (*config.C*). The dataset for *config.A* can be used for non-adversarial and adversarial supervised training schemes, and the other two datasets supported semi-supervised adversarial training.

### B. Implementation and Training Model Parameters

The model was implemented in Pytorch and trained on two RTX 2080 Ti GPUs, and we expedited the training process by data parallelism. For  $S$ -net, we used Adam optimizer [37] with an initial learning rate of  $5 \times 10^{-4}$  and polynomial learning rate scheduler with a power of 0.9. For  $D$ -net, we used Adam optimizer with an initial learning rate of  $10^{-4}$ , and the same learning rate scheduler as for  $S$ -net. For the other parameters in Eq. 11, we set  $\lambda_{adv} = 0.01$  or 0.001 for annotated and un-annotated data, respectively, and  $\lambda_{semi} = 0.1$  as suggested in [30].

In the semi-supervised adversarial learning described in III.D and III.E, we used both annotated and un-annotated data (*config.B* or *config.C*) for training. Following [30], we pre-trained *S-net* and *D-net* with only labeled data for 5000 iterations before semi-supervised training started. The pre-training iterations can help stabilize the randomly initiated model. After pre-trained *S-net* and *D-net*, we randomly interleaved annotated and un-annotated data for semi-supervised training [30]. We trained the semi-supervised adversarial model on *config.B* and *config.C* dataset for 40k iterations with batch size 2.

We also implemented and trained several baseline models for model comparison and evaluation (Table I): 1) *3d\_res\_Unet* is a vanilla residual U-net model as proposed in [2]; 2) *3d\_res\_Unet\_aux* is the *res\_Unet* upgraded with auxiliary classifiers; 3) *3d\_res\_Unet\_aux\_adv* is the adversarial learning version of *3d\_res\_Unet\_aux*; and 4) *3d\_res\_Unet\_aux\_adv\_semi* is the complete version of our proposed method. The first three models can be trained with *config.A*, and only the complete version can be built with *config.B* and *config.C*.

Table I: Experiments for model comparison.

Experiment No.	Model	Dataset
1	<i>3d_res_Unet</i> [2]	90 labeled
2	<i>3d_res_Unet_aux</i>	90 labeled

3	<i>3d_res_Unet_aux_adv</i>	90 labeled
4	<i>3d_res_Unet_aux_adv_semi</i> (our method)	60 labeled & 30 unlabeled
5	<i>3d_res_Unet_aux_adv_semi</i> (our method)	90 labeled & 30 unlabeled

### C. Evaluation Metrics

Four evaluation metrics were used in our experiments: dice similarity coefficient [38], average Hausdorff distance [39], average surface Hausdorff distance [40], and relative volume difference [40].

Dice similarity coefficient (DSC) is a widely used segmentation metric in medical imaging:

$$DSC = \frac{2 \times |True \cap Pred|}{|True| + |Pred|}, \quad (13)$$

where  $|True|$  and  $|Pred|$  are the number of voxels in the ground-truth and prediction, respectively [7].

The average Hausdorff distance (AHD) [5] measures the maximal average point-wise distance from points in  $X$  to the nearest point in  $Y$ , and the average point-wise distance from points in  $Y$  to the nearest point in  $X$ :

$$AHD(X, Y) = \max(\frac{1}{|X|} \sum_{x \in X} \min_{y \in Y} d(x, y), \frac{1}{|Y|} \sum_{y \in Y} \min_{x \in X} d(y, x)), \quad (14)$$

where  $X$  and  $Y$  are the voxel sets of the ground-truth and prediction volume, respectively, and  $d(x, y)$  is the Euclidean distance from point  $x$  to point  $y$ .

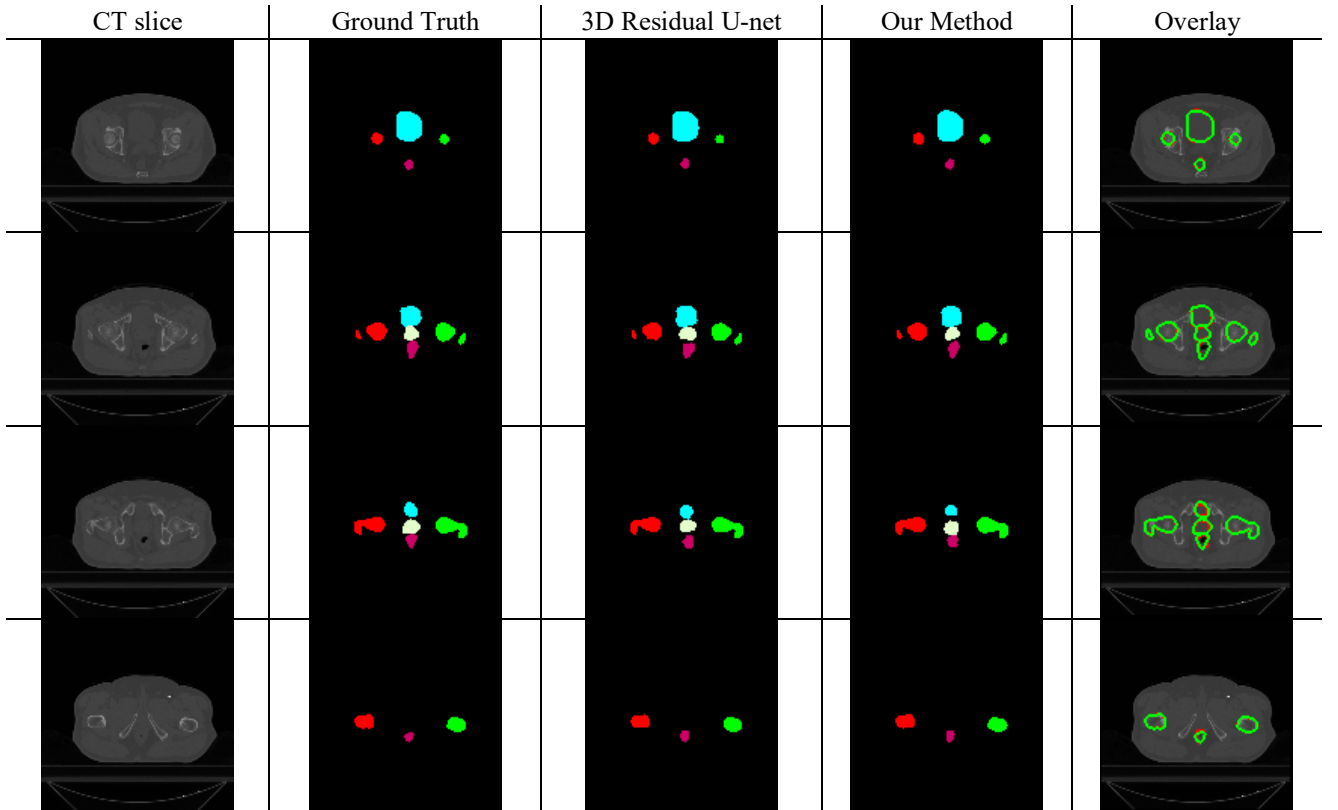


Fig. 2. Exhibition of segmentation results comparison. Five columns are CT slices, ground-truth label masks (bladder in light blue, prostate in beige, rectum in purple, and femurs in red and green), prediction label masks of the baseline and our method, and contour overlay (ground truth in green and prediction in red) of the proposed method. The four slices are selected from the same test case and ordered from superior to inferior.

The Average Surface Hausdorff Distance (ASHD) [5] is the symmetrical average point-wise distance between a point on one surface to the nearest point on the other surface:

$$ASHD(X, Y) = \frac{1}{2} \left( \frac{1}{|X|} \sum_{x \in X} \min_{y \in Y} d(x, y) + \frac{1}{|Y|} \sum_{y \in Y} \min_{x \in X} d(y, x) \right), \quad (15)$$

where  $X$  and  $Y$  are the voxel sets of the ground-truth and prediction surface, respectively, and  $d(x, y)$  is the Euclidean distance from point  $x$  to point  $y$ .

## V. RESULTS

### A. Model Evaluation

We evaluated the performance of our new method and the baseline methods by 10-fold cross-validation (Fig. 2). The proposed method can generate accurate contours for all five targeted OARs (Table II), and the contours closely resemble the ground-truth (Fig. 2). Our proposed approach achieves nearly 100% accuracy on both femurs (Table II) thanks to their high contrast with the background on CT images. However, the prostate, bladder, and rectum are more challenging to segment due to their low contrast and fuzzy boundaries. Despite the low contrast, our approach generates high-quality segmentation contours that closely align with the ground-truth. Compared to manual segmentation that typically takes 20-30 minutes per patient for the prostate alone, our approach can segment five OARs in 10 seconds per patient. The results suggest that the new approach can improve the quality of routine clinical practice by rapidly producing accurate contours with high efficiency.

### B. Effectiveness of Semi-supervised Adversarial Learning

The lack of data has always been a severe bottleneck for most medical imaging projects and often compromises the outcome of analytic models, particularly those based on deep learning [6]. A notable feature of the new method is its ability to generate synthesized data to adequately address insufficient training data and its semi-supervised learning capability to accommodate annotated and un-annotated data to improve overall performance. Importantly, since the new method can utilize un-annotated images, we can use fewer manually annotated cases, thus significantly reduce overall labor and cost.

We compared the performance of the proposed approach with baseline methods to show that the proposed approach achieves comparable results with less annotated data and better results with the same amount of annotated data (Table II).

Experiments 1 and 2 were designed to measure the effectiveness of auxiliary classifiers. Even though the prostate and rectum are challenging to segment due to their low contrast level and variations in size and shape, using auxiliary classifiers in the new method can improve performance on the prostate and rectum (Table I). With auxiliary classifiers that perform segmentation on feature maps of multiple scales, the model generated better contours for organs of various shapes and sizes. Experiments 2 and 3 were used to analyze the effectiveness of adversarial training. The results showed the performance on the prostate and rectum was improved with the adversarial training scheme, which proved the effectiveness of adding style-wise loss into the loss function.

Table II: Experiment results from 10-fold cross-validation. We evaluated the performance with four metrics: dice similarity coefficient (DSC), average Hausdorff distance (AHD), average surface Hausdorff distance (ASHD), and relative volume difference (VD) on five OARs: prostate, bladder, rectum, left femur (Femur\_L) and right femur (Femur\_R). The best score of each metric on each organ is colored in red.

Experiment No.	Model	Dataset	Prostate DSC AHD(mm) ASHD(mm) VD(%)	Bladder DSC AHD(mm) ASHD(mm) VD(%)	Rectum DSC AHD(mm) ASHD(mm) VD(%)	Femur_L DSC AHD(mm) ASHD(mm) VD(%)	Femur_R DSC AHD(mm) ASHD(mm) VD(%)
1	<i>3d_res_Unet</i> [2]	90 labeled	0.85(±0.12) 0.34(±0.13) 0.80(±0.17) -11.13	0.95(±0.10) 0.12(±0.10) 0.50(±0.23) -0.98	0.84(±0.12) 0.40(±0.46) 0.68(±0.31) -7.72	0.97(±0.01) 0.06(±0.04) 0.27(±0.16) -1.62	0.97(±0.01) 0.04(±0.01) 0.18(±0.05) -1.89
2	<i>3d_res_Unet_aux</i>	90 labeled	0.86(±0.14) 0.33(±0.16) 0.78(±0.17) -4.27	0.95(±0.07) 0.10(±0.10) 0.42(±0.17) +2.92	0.86(±0.19) 0.39(±0.32) 0.65(±0.30) -1.52	0.97(±0.01) 0.04(±0.02) 0.25(±0.10) -1.24	0.97(±0.01) 0.04(±0.02) 0.25(±0.18) -1.27
3	<i>3d_res_Unet_aux_adv</i>	90 labeled	0.87(±0.15) 0.31(±0.16) 0.77(±0.21) -3.07	0.96(±0.07) 0.09(±0.08) 0.41(±0.14) +3.22	0.87(±0.13) 0.36(±0.35) 0.63(±0.27) -0.97	0.97(±0.01) 0.04(±0.02) 0.22(±0.09) -0.53	0.97(±0.01) 0.06(±0.07) 0.23(±0.16) -0.97
4	<i>3d_res_Unet_aux_adv_semi</i> (our method)	60 labeled & 30 unlabeled	0.86(±0.13) 0.36(±0.20) 0.82(±0.15) -4.45	0.96(±0.07) 0.12(±0.11) 0.51(±0.17) +3.24	0.86(±0.12) 0.36(±0.34) 0.66(±0.31) -1.01	0.97(±0.01) 0.05(±0.03) 0.21(±0.08) -0.66	0.97(±0.01) 0.06(±0.08) 0.22(±0.11) -0.99
5	<i>3d_res_Unet_aux_adv_semi</i> (our method)	90 labeled & 30 unlabeled	0.90(±0.09) 0.23(±0.11) 0.62(±0.15) -4.38	0.96(±0.06) 0.12(±0.11) 0.45(±0.22) +0.80	0.87(±0.11) 0.28(±0.17) 0.57(±0.18) -5.46	0.97(±0.01) 0.04(±0.02) 0.22(±0.09) -0.01	0.97(±0.01) 0.04(±0.02) 0.19(±0.07) -0.64



We designed experiments 3 and 4 to test if our method can achieve comparable or even better results with less annotated data points. The results showed that discarding 1/3 of the annotations would not hurt the performance much with the proposed semi-supervised learning algorithm. With Experiments 3 and 4, we proved the new method required less effort for data annotation.

We also expected additional synthesized CT images to improve the performance with the same amount of annotated data. Thus, we introduced experiments 3 and 5 to test if our model can achieve better performance with PGGAN-synthesized data augmentation. Results in Table II proved the effectiveness of introducing semi-supervised loss and training with extra synthesized data under the adversarial learning scheme.

Despite the performance testing, we also tested the data robustness of our semi-supervised learning scheme. In experiment 4, the un-annotated cases utilized were real CT images without annotations. However, in experiment 5, the 30 un-annotated cases utilized were synthesized by the PGGAN method. As indicated by the results from experiments 4 and 5, we proved the effectiveness of PGGAN-aided CT synthesis. More importantly, both real un-annotated images (Exp. 4) and PGGAN-synthesized un-annotated images (Exp. 5) were eligible to support the semi-supervised part of our learning algorithm.

### C. Model Comparison

We compared the performance of our model with state-of-the-art models for pelvic CT segmentation, including one multi-atlas based model [1] and four deep learning-based models. Deep Dilated CNN [3] and 2D U-net [5] are end-to-end models, and 2D U-net Localization plus 3D U-net Segmentation [4] is

a two-step ROI segmentation approach. The new approach achieved comparable or better performance than current state-of-the-art methods (Table III). The proposed method outperformed the multi-atlas based model [1] and Deep Dilated CNN method with higher DSCs on all OARs. The 2D U-net and 2D U-net Localization plus 3D U-net Segmentation are ROI segmentation methods so that multiple networks are trained for different OARs catering to different shapes, sizes, and contrast levels. The method required one 2D localization network and four 3D segmentation networks with different architectural designs to segment four different OARs, which increased the difficulty of implementation. Our proposed method achieved similar DSCs on all OARs as the two ROI segmentation methods. However, unlike the ROI segmentation model that trains one segmentation network for each organ, our model performed an end-to-end segmentation method and segmented all organs with one trained network. Compared to the ARPM-net, which also segmented all OARs within one forward propagation [7], our new method achieves better DSCs, AHDs, and ASHDs on the prostate and rectum. Our new method was trained and tested with the same dataset as the ARPM-net, and our semi-supervised adversarial learning scheme supported by PGGAN-aided CT synthesis significantly lowered HDs and AHDs by utilizing extra style-wise loss for learning.

Despite the performance increase on multiple OARs, our method incorporated a semi-supervised adversarial learning scheme and tackled the lack-of-data problem by training with un-annotated data supplied by PGGAN-aided data synthesis.

## VI. CONCLUSION AND DISCUSSION

The research was motivated in part to address the problem of the lack of data in medical imaging. In particular, we proposed

Table III: Model performance on testing data. The best score of each metric on each organ is colored in red. Note that relative volume difference is not listed because the metric was not used in most of compared methods.

	<b>Prostate</b> DSC AHD(mm) ASHD(mm)	<b>Bladder</b> DSC AHD(mm) ASHD(mm)	<b>Rectum</b> DSC AHD(mm) ASHD(mm)	<b>Femur_L</b> DSC AHD(mm) ASHD(mm)	<b>Femur_R</b> DSC AHD(mm) ASHD(mm)
<i>Multi-atlas Based Segmentation</i> [1] (2014)	0.85( $\pm 0.004$ ) - -	0.92( $\pm 0.002$ ) - -	0.80( $\pm 0.007$ ) - -	N/A	N/A
<i>Deep Dilated CNN</i> [3] (2017)	0.88 - -	0.93 - -	0.62 - -	0.92 - -	0.92 - -
<i>2D U-net</i> [5] (2018)	0.88( $\pm 0.12$ ) 0.4( $\pm 0.7$ ) 1.2( $\pm 0.9$ )	0.95( $\pm 0.04$ ) 0.4( $\pm 0.6$ ) 1.1( $\pm 0.8$ )	<b>0.92(<math>\pm 0.06</math>)</b> <b>0.2(<math>\pm 0.3</math>)</b> 0.8( $\pm 0.6$ )	N/A	N/A
<i>2D U-net Localization, 3D U-net Segmentation</i> [4] (2018)	<b>0.90(<math>\pm 0.02</math>)</b> 5.3( $\pm 2.8$ ) <b>0.7(<math>\pm 0.5</math>)</b>	0.95( $\pm 0.02$ ) 17.0( $\pm 14.6$ ) 0.5( $\pm 0.7$ )	0.84( $\pm 0.04$ ) 4.9( $\pm 3.9$ ) 0.8( $\pm 0.7$ )	0.96( $\pm 0.03$ ) - -	0.95( $\pm 0.01$ ) - -
<i>ARPM-net</i> [7] (2020)	0.88( $\pm 0.11$ ) 1.58( $\pm 1.77$ ) 2.11( $\pm 2.03$ )	<b>0.97(<math>\pm 0.07</math>)</b> 1.91( $\pm 1.29$ ) 2.36( $\pm 2.43$ )	0.86( $\pm 0.12$ ) 3.14( $\pm 2.39$ ) 3.05( $\pm 2.11$ )	<b>0.97(<math>\pm 0.01</math>)</b> 1.76( $\pm 1.57$ ) 1.99( $\pm 1.66$ )	<b>0.97(<math>\pm 0.01</math>)</b> 1.92( $\pm 1.01$ ) 2.00( $\pm 2.07$ )
<i>3d_res_Unet_aux_adv_semi</i> (our method)	0.90( $\pm 0.12$ ) <b>0.27(<math>\pm 0.13</math>)</b> 0.77( $\pm 0.20$ )	0.95( $\pm 0.05$ ) <b>0.11(<math>\pm 0.13</math>)</b> <b>0.47(<math>\pm 0.23</math>)</b>	0.87( $\pm 0.10$ ) 0.30( $\pm 0.19$ ) <b>0.63(<math>\pm 0.21</math>)</b>	<b>0.97(<math>\pm 0.01</math>)</b> <b>0.04(<math>\pm 0.01</math>)</b> <b>0.24(<math>\pm 0.11</math>)</b>	<b>0.97(<math>\pm 0.01</math>)</b> <b>0.04(<math>\pm 0.02</math>)</b> <b>0.18(<math>\pm 0.06</math>)</b>



a novel semi-supervised adversarial segmentation approach for 3D male pelvic CT semantic segmentation, where we may not have sufficient training examples. We introduced in the new method semi-supervised adversarial learning that can utilize synthesized un-annotated CT images. We cast semantic segmentation as a problem of adversarial learning for data generation and semi-supervised learning to make use of both annotated and un-annotated data. We measured the new method with four metrics: dice similarity coefficient, average Hausdorff distance, average surface Hausdorff distance, and relative volume difference. Evaluation results showed that our new method achieved state-of-the-art performance. The consistency and effectiveness were tested by 10-fold-cross validation on real 3D pelvic CT images.

The semi-supervised adversarial learning method outperformed the baseline methods with the same amount of annotated data and achieved comparable performance with less annotated data. The proposed method can produce high-quality contours for five organ-at-risks (the prostate, bladder, rectum, left femur, and right femur).

The new method can be improved. Firstly, like most adversarial learning models, the hyperparameters of our proposed model are delicate to tune. Training the model may encounter mode collapse, and it is challenging to balance the learning progress of the segmentation network and the discriminator. Secondly, the potential of progressive growth GAN [27] has not been fully exploited. It can potentially generate new data with corresponding ground-truth annotations[17], and we plan to investigate how synthesized annotated CT images can aid the learning process.

## ACKNOWLEDGMENT

The work was supported in part by Varian Medical Systems through a research grant. We obtained the Washington University of St. Louis institutional review board (IRB) approval for this study and the patient data used in the study.

## REFERENCES

- [1] O. Acosta, J. Dowling, G. Drean, A. Simon, R. De Crevoisier, and P. Haigron, "Multi-atlas-based segmentation of pelvic structures from CT scans for planning in prostate cancer radiotherapy," *Abdomen and Thoracic Imaging*, pp. 623-656: Springer, 2014.
- [2] Z. Zhang, Q. Liu, and Y. Wang, "Road extraction by deep residual u-net," *IEEE Geoscience and Remote Sensing Letters*, vol. 15, no. 5, pp. 749-753, 2018.
- [3] K. Men, J. Dai, and Y. Li, "Automatic segmentation of the clinical target volume and organs at risk in the planning CT for rectal cancer using deep dilated convolutional neural networks," *Medical physics*, vol. 44, no. 12, pp. 6377-6389, 2017.
- [4] A. Balagopal, S. Kazemifar, D. Nguyen, M.-H. Lin, R. Hannan, A. Owangi, and S. Jiang, "Fully automated organ segmentation in male pelvic CT images," *Physics in Medicine & Biology*, vol. 63, no. 24, pp. 245015, 2018.
- [5] S. Kazemifar, A. Balagopal, D. Nguyen, S. McGuire, R. Hannan, S. Jiang, and A. Owangi, "Segmentation of the prostate and organs at risk in male pelvic CT images using deep learning," *Biomedical Physics & Engineering Express*, vol. 4, no. 5, pp. 055003, 2018.
- [6] S. Wang, D. Nie, L. Qu, Y. Shao, J. Lian, Q. Wang, and D. Shen, "CT Male Pelvic Organ Segmentation via Hybrid Loss Network With Incomplete Annotation," *IEEE Transactions on Medical Imaging*, vol. 39, no. 6, pp. 2151-2162, 2020.
- [7] Z. Zhang, T. Zhao, H. Gay, W. Zhang, and B. Sun, "ARPM-net: A novel CNN-based adversarial method with Markov Random Field enhancement for prostate and organs at risk segmentation in pelvic CT images," *arXiv preprint arXiv:2008.04488*, 2020.
- [8] I. Goodfellow, Y. Bengio, A. Courville, and Y. Bengio, *Deep learning*: MIT press Cambridge, 2016.
- [9] F. Martínez, E. Romero, G. Dréan, A. Simon, P. Haigron, R. De Crevoisier, and O. Acosta, "Segmentation of pelvic structures for planning CT using a geometrical shape model tuned by a multi-scale edge detector," *Physics in Medicine & Biology*, vol. 59, no. 6, pp. 1471, 2014.
- [10] Q. Dou, L. Yu, H. Chen, Y. Jin, X. Yang, J. Qin, and P.-A. Heng, "3D deeply supervised network for automated segmentation of volumetric medical images," *Medical image analysis*, vol. 41, pp. 40-54, 2017.
- [11] Y. Gao, Y. Shao, J. Lian, A. Z. Wang, R. C. Chen, and D. Shen, "Accurate segmentation of CT male pelvic organs via regression-based deformable models and multi-task random forests," *IEEE transactions on medical imaging*, vol. 35, no. 6, pp. 1532-1543, 2016.
- [12] B. Wang, Y. Lei, T. Wang, X. Dong, S. Tian, X. Jiang, A. B. Jani, T. Liu, W. J. Curran, and P. Patel, "Automated prostate segmentation of volumetric CT images using 3D deeply supervised dilated FCN." p. 109492S.
- [13] Y. Fu, T. R. Mazur, X. Wu, S. Liu, X. Chang, Y. Lu, H. H. Li, H. Kim, M. C. Roach, and L. Henke, "A novel MRI segmentation method using CNN - based correction network for MRI - guided adaptive radiotherapy," *Medical physics*, vol. 45, no. 11, pp. 5129-5137, 2018.
- [14] K. H. Cha, L. Hadjiiski, R. K. Samala, H. P. Chan, E. M. Caoili, and R. H. Cohan, "Urinary bladder segmentation in CT urography using deep - learning convolutional neural network and level sets," *Medical physics*, vol. 43, no. 4, pp. 1882-1896, 2016.
- [15] O. Ronneberger, P. Fischer, and T. Brox, "U-net: Convolutional networks for biomedical image segmentation." pp. 234-241.
- [16] I. Goodfellow, J. Pouget-Abadie, M. Mirza, B. Xu, D. Warde-Farley, S. Ozair, A. Courville, and Y. Bengio, "Generative adversarial nets." pp. 2672-2680.
- [17] C. Bowles, L. Chen, R. Guerrero, P. Bentley, R. Gunn, A. Hammers, D. A. Dickie, M. V. Hernández, J. Wardlaw, and D. Rueckert, "Gan augmentation: Augmenting training data using generative adversarial networks," *arXiv preprint arXiv:1810.10863*, 2018.
- [18] L. Ma, R. Guo, G. Zhang, F. Tade, D. M. Schuster, P. Nieh, V. Master, and B. Fei, "Automatic segmentation of the prostate on CT images using deep learning and multi-atlas fusion." p. 1013320.
- [19] C. Lu, Y. Zhang, N. Birkbeck, J. Zhang, T. Kohlberger, C. Tietjen, T. Boettger, J. S. Duncan, and S. K. Zhou, "Precise segmentation of multiple organs in CT volumes using learning-based approach and information theory." pp. 462-469.
- [20] M. W. Macomber, M. Phillips, I. Tarapov, R. Jena, A. Nori, D. Carter, L. Le Folgoc, A. Criminisi, and M. J. Nyflot, "Autosegmentation of prostate anatomy for radiation treatment planning using deep decision forests of radiomic features," *Physics in Medicine & Biology*, vol. 63, no. 23, pp. 235002, 2018.
- [21] X. Dong, Y. Lei, S. Tian, T. Wang, P. Patel, W. J. Curran, A. B. Jani, T. Liu, and X. Yang, "Synthetic MRI-aided multi-organ segmentation on male pelvic CT using cycle consistent deep attention network," *Radiotherapy and Oncology*, vol. 141, pp. 192-199, 2019.
- [22] X. Ma, L. M. Hadjiiski, J. Wei, H. P. Chan, K. H. Cha, R. H. Cohan, E. M. Caoili, R. Samala, C. Zhou, and Y. Lu, "U - Net based deep learning bladder segmentation in CT urography," *Medical physics*, vol. 46, no. 4, pp. 1752-1765, 2019.
- [23] J. Long, E. Shelhamer, and T. Darrell, "Fully convolutional networks for semantic segmentation." pp. 3431-3440.
- [24] N. Ibtchaz, and M. S. Rahman, "MultiResUNet: Rethinking the U-Net architecture for multimodal biomedical image segmentation," *Neural Networks*, vol. 121, pp. 74-87, 2020.
- [25] I. Goodfellow, "NIPS 2016 tutorial: Generative adversarial networks," *arXiv preprint arXiv:1701.00160*, 2016.
- [26] M. Mirza, and S. Osindero, "Conditional generative adversarial nets," *arXiv preprint arXiv:1411.1784*, 2014.

- [27] T. Karras, T. Aila, S. Laine, and J. Lehtinen, "Progressive growing of gans for improved quality, stability, and variation," *arXiv preprint arXiv:1710.10196*, 2017.
- [28] L. Chongxuan, T. Xu, J. Zhu, and B. Zhang, "Triple generative adversarial nets." pp. 4088-4098.
- [29] P. Luc, C. Couprie, S. Chintala, and J. Verbeek, "Semantic segmentation using adversarial networks," *arXiv preprint arXiv:1611.08408*, 2016.
- [30] W.-C. Hung, Y.-H. Tsai, Y.-T. Liou, Y.-Y. Lin, and M.-H. Yang, "Adversarial learning for semi-supervised semantic segmentation," *arXiv preprint arXiv:1802.07934*, 2018.
- [31] K. He, X. Zhang, S. Ren, and J. Sun, "Deep residual learning for image recognition." pp. 770-778.
- [32] L.-C. Chen, G. Papandreou, I. Kokkinos, K. Murphy, and A. L. Yuille, "Deeplab: Semantic image segmentation with deep convolutional nets, atrous convolution, and fully connected crfs," *IEEE transactions on pattern analysis and machine intelligence*, vol. 40, no. 4, pp. 834-848, 2017.
- [33] L. Yu, X. Yang, H. Chen, J. Qin, and P.-A. Heng, "Volumetric convnets with mixed residual connections for automated prostate segmentation from 3D MR images." pp. 36-72.
- [34] Z. Zhang, L. Yang, and Y. Zheng, "Translating and segmenting multimodal medical volumes with cycle-and shape-consistency generative adversarial network." pp. 9242-9251.
- [35] A. Krizhevsky, I. Sutskever, and G. E. Hinton, "Imagenet classification with deep convolutional neural networks." pp. 1097-1105.
- [36] H. Noh, S. Hong, and B. Han, "Learning deconvolution network for semantic segmentation." pp. 1520-1528.
- [37] D. P. Kingma, and J. Ba, "Adam: A method for stochastic optimization," *arXiv preprint arXiv:1412.6980*, 2014.
- [38] V. Thada, and V. Jaglan, "Comparison of jaccard, dice, cosine similarity coefficient to find best fitness value for web retrieved documents using genetic algorithm," *International Journal of Innovations in Engineering and Technology*, vol. 2, no. 4, pp. 202-205, 2013.
- [39] D. P. Huttenlocher, G. A. Klanderman, and W. J. Rucklidge, "Comparing images using the Hausdorff distance," *IEEE Transactions on pattern analysis and machine intelligence*, vol. 15, no. 9, pp. 850-863, 1993.
- [40] A. A. Taha, and A. Hanbury, "Metrics for evaluating 3D medical image segmentation: analysis, selection, and tool," *BMC medical imaging*, vol. 15, no. 1, pp. 29, 2015.